Journal of Materials Chemistry A

Accepted Manuscript

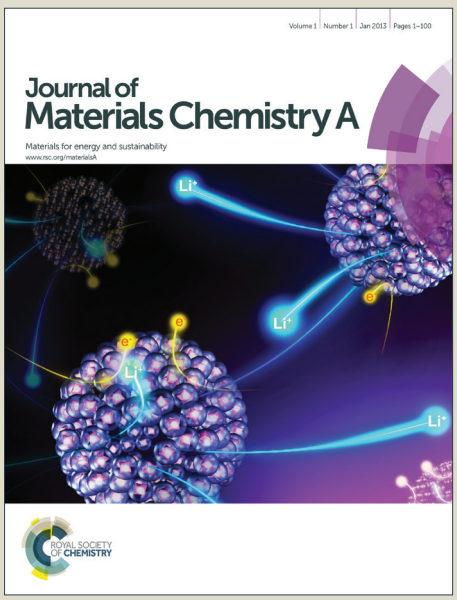

ROYAL SOCIETY OF CHEMISTRY

www.rsc.org/materialsA

Journal Name

RSCPublishing

ARTICLE

Self-assembly of monodispersed hierarchically porous Beta-SBA-15 with different morphologies and their hydro-upgrading performances of FCC gasoline

Cite this: DOI: 10.1039/xoxxoooooox

Received ooth January 2012,
Accepted ooth January 2012

DOI: 10.1039/xoxxoooooox

www.rsc.org/

Daowei Gao,[a] Aijun Duan,*[a] Xin Zhang,*[a] Kebin Chi,[b] Zhen Zhao,[a] Jianmei Li,[c] Yuchen Qin,[a] Xilong Wang,[a] Chunming Xu[a]

Micro-mesoporous Beta-SBA-15 materials with platelet, sphere, short-rod and long-rod morphologies were in-situ synthesized and used as the catalyst supports for hydro-upgrading of FCC gasoline. The characterization results revealed that the Beta-SBA-15 composites possessed both SBA-15 and Beta structures. And the materials with different morphologies exhibited different Brönsted and Lewis acid sites and pore sizes due to their corresponding synthesis conditions. The platelet Beta-SBA-15 which possessed the short mesochannels with large pore diameter had high diffusion ability. The sphere Beta-SBA-15 with more mesopore cavities, high surface area and suitable acidity exhibited outstanding isomerization and aromatization abilities. The catalytic results confirmed that the platelet CoMo/ABS-PL exhibited the high hydrodesulfurization (HDS) conversion (97.6 %) while the sphere CoMo/ABS-SP catalyst showed the superior research octane number (RON) preservation ability, which were better than those of CoMo/ABS-SR (short-rod) and CoMo/ABS-LR (long-rod) catalysts. The excellent hydrodesulfurization, isomerization and aromatization abilities of CoMo/ABS-PL and CoMo/ABS-SP were attributed to the special morphology, mesochannel and the appropriate acidity properties of the catalysts. Thus, the as-synthesized platelet and sphere Beta-SBA-15 materials have potential application in FCC gasoline hydro-upgrading.

1 Introduction

Sulfur-containing compounds in gasoline are one of the major sources of air pollutants and must be reduced in accord with the strict fuel specifications (even as low as about 0 ppm in the near future).[1-3] FCC gasoline is the major blending components in gasoline pool and occupies more than 90% of total sulfur content in the refinery gasoline in China. Therefore, the deep reduction of sulfur content in FCC gasoline is the most effective method to produce ultra clean gasoline. The hydro-upgrading process is one of the most widely used techniques for sulfur removal from FCC gasoline in the refinery.[4, 5] However, the conventional alumina-supported CoMo catalyst of hydro-upgrading has a high hydrodesulfurization (HDS) conversion but with a great loss of the research octane number (RON). Since the conventional γ-Al_2O_3 support has low acidity, large pore size distribution and strong interaction with metal oxide precursor, thus it faces up with great challenge to meet the stringent specifications.[6, 7] How to balance the deep hydrodesulfurization efficiency and good RON preservablity will be siginificant for FCC gasoline hydro-upgrading. Therefore, the exploration of novel supports with excellent catalytic performance for HDS and RON preserving ability of FCC gasoline becomes an important issue.

The catalytic hydro-upgrading of FCC gasoline over various catalysts are correlated to the acidity, pore size and surface area of the catalysts. Since the zeolites ZSM-5, β and L have a large number of B and L acid sites and high hydrothermal stability, they can be the ideal support additive for isomerization or aromatization reactions.[8-10] However, the small pores of zeolites limit its wide application in some processes involving large reactant molecules. Mesoporous silica materials with high surface areas and well ordered pore structures can eliminate the diffusion hindrance of microporous zeolites, and they may have potential applications in the catalytic conversion processes of large reactant molecules.[11-15] Nevertheless, the weak acidity and poor hydrothermal stability of mesoporous silica materials are also the barriers. The design and development of micro/mesoporous composite materials aim at the combination of the advantage of microporous and mesoporous materials, and also overcome the disadvantages of weak acidity of

mesoporous zeolites and small pore sizes of microporous zeolites. For instance, Zhang et al[16] prepared a novel NiMo catalyst supported on micro-mesoporous Beta-KIT-6 (BK), and the DBT HDS results showed that NiMo/Beta-KIT-6 with superior mass transfer ability exhibited a higher activity than NiMo/γ-Al_2O_3. And the acidity of NiMo/BK enhanced the activity of the direct desulfurization pathway more significantly than that of the hydrogenation pathway.

Besides the acidity and pore size, the morphology and mesochannel of the supports also have effect on the catalytic performance.[12, 17-19] The shape and meschannel of the catalysts are crucial factors for the dispersion of active metal species and the diffusion of the reactants and the products. Chen et al[20] reported that the functionalized mesoporous SBA-15 with platelet morphology were superior to the conventional SBA-15 materials with rod or fiber morphologies in facilitating the molecular diffusion and reducing the pore blockage. Katiyar et al.[21] also prepared SBA-15 mesoporous silica with sphere particles which had a higher pore volume than the fibrous particles. It is now apparent that the catalytic properties are related to the morphology of the materials. So far, many researchers have devoted to the synthesis of mesoporous materials with well-defined morphology.[22-25] However, no detailed studies have been made to synthesize shape-controlled Beta-SBA-15 micro/mesoporous composite materials and investigate the effect of its morphology on the catalytic activity. Therefore, the synthesis of monodispersed hierarchically porous Beta-SBA-15 with different morphologies and the study of the catalytic behavior of as-synthesized materials on FCC gasoline hydro-upgrading are of great significant.

In this research, a series of Beta-SBA-15 materials with platelet, sphere, short-rod and long-rod morphologies were successfully synthesized by a two-step hydrothermal crystallization method using pluronic P123 triblock copolymer and cosurfactant of cetyltrimethylammonium bromide (CTAB) as structure-directing agents (SDA). The composite materials were used as the support and the corresponding catalysts were evaluated in the hydro-upgrading of FCC gasoline, while the conventional CoMo/γ-Al_2O_3 catalyst was taken as the reference. In addition, the physicochemical properties of the supports and catalysts were analysed by various characterization techniques. The catalytic multifunction performances, including HDS and RON preservation of the series catalysts supported on Beta-SBA-15 composites, were systematically investigated. The effects of different morphologies of Beta-SBA-15 on the catalytic performances of FCC gasoline hydro-upgrading were also discussed. Furthermore, the relationship of the amount of acid sites and the isomerization (ISO) and aromatization (ARO) selectivities were also explored.

2 Experimental

2.1 Preparation of the supports

Beta-SBA-15 with different morphologies was prepared as following procedure and the synthetic process is displayed in Scheme 1. Firstly, zeolite Beta nanocrystal clusters were synthesized with the molar ratio of 1.0 Al_2O_3:60.0 SiO_2:1.4 Na_2O:15.0 TEAOH:360.0 H_2O. A zeolite Beta seed solution was prepared by adding 0.2 g of NaOH, 0.4 g of $NaAlO_2$, and 21.4 g of tetraethylorthosilicate (TEOS) into 25.9 g of an aqueous TEAOH solution (25%). The mixture was homogenized by stirring for 4 h, and then aged at 140 °C for 12 h to obtain a zeolite Beta seed solution. Secondly, 2 g P123 (Sigma–Aldrich) was dissolved in the mixture of H_2O and hydrochloric acid solution, then a certain amount of precursor zeolite Beta seed and TEOS were added to the above solution with vigorous string. The reaction composition of short-rod Beta-SBA-15 was 1.0 Al_2O_3:120.0 SiO_2:1.0 P123:353.0 HCl:12254.0 H_2O. Then the mixture was stirred at 40 °C for 1 h under confined stirring rate and further maintained at static condition for 24 h. The gel solution was transferred into a Teflon bottle and heated at 100 °C for 24 h without stirring. The preparation of long-rod Beta-SBA-15 was similar with short-rod SBA-15 with a mixture composition of 1.0 Al_2O_3:120.0 SiO_2:1.0 P123:382.0 HCl:10621.0 H_2O. But the stirring temperature was 55 °C. A small amount of Zr(IV) ions was also added in the mixture during the synthesis of platelet Beta-SBA-15 material, resulting in a gel of Al_2O_3:SiO_2:P123:$ZrOCl_2$•8H_2O:HCl:H_2O with a mole ratio of 1.0:120.0:1.0:3.0:441.0:12255.0. And the synthetic method was the same as short-rod SBA-15. Sphere Beta-SBA-15 was synthesized by using CTAB (Aldrich) as a cosurfactant according to the above procedure with a composition of 1.0 Al_2O_3:120.0 SiO_2:1.0 P123:3.2 CTAB:265.0 HCl:10417.0 H_2O. After the above product cooling to the room temperature, Beta-SBA-15 with different morphologies was recovered by filtering and drying at room temperature in air. Then, all samples were calcined at 550 °C for 6 h to remove the copolymer template. The Beta-SBA-15 with short-rod, long-rod, platelet and sphere

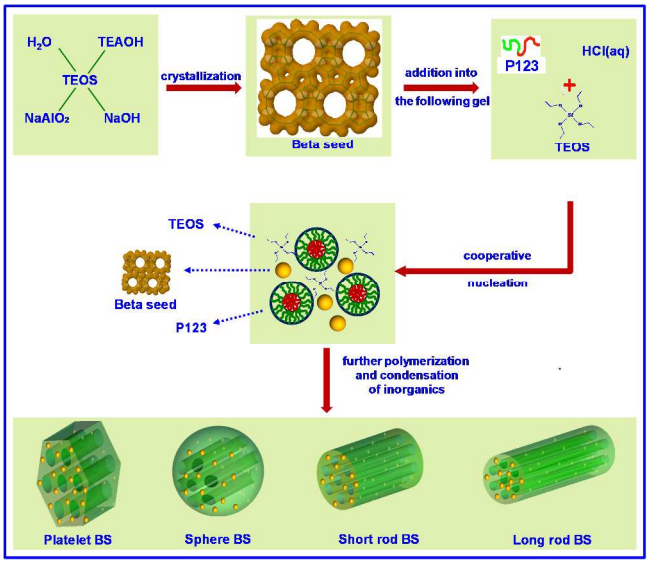

Scheme 1. Preparation of the monodispersed hierarchically porous Beta-SBA-15 with different morphologies.

morphologies were denoted as BS-SR, BS-LR, BS-PL and BS-SP, respectively.

2.2 Preparation of the catalysts

The supports were prepared by using the hierarchically porous Beta-SBA-15 materials with different morphologies as additives covering 40wt.% in support and the residue was γ-Al_2O_3 (Aluminum Corporation of China Limited). Supported CoMo catalysts were prepared by two-step incipient-wetness impregnation of ammonium heptamolybdate and cobalt nitrate. The samples were dried at 110 ^oC for 24 h, and then calcined at 550 ^oC for 6 h in air after each impregnation step. The catalysts were crushed into 0.3–0.5 mm particles. The prepared catalysts were denoted as CoMo/ABS-PL (CoMo/BS-PL-γ-Al_2O_3), CoMo/ABS-SP (CoMo/BS-SP-γ-Al_2O_3), CoMo/ABS-SR (CoMo/BS-SR-γ-Al_2O_3) and CoMo/ABS-LR (CoMo/BS-LR-γ-Al_2O_3). The traditional catalyst of CoMo/γ-Al_2O_3 was used as a reference catalyst. The loading of CoO (5wt.%) and MoO_3 (10wt.%) was kept the same on the above five catalysts. In addition, the other two catalysts with different loading of CoO were also prepared. CoMo/ABS-PLM (CoMo/BS-PL-Middle-γ-Al_2O_3) and Mo/ABS-PL (Mo/BS-PL-γ-Al_2O_3) with the loadings of CoO were 2.5wt.% and 0wt.%, respectively, and the loading of MoO_3 (10wt.%) was the same as the above catalysts.

2.3 Characterization of supports and catalysts

The small-angle X-ray diffraction patterns were recorded on a Bruker D8 Advance Powder diffractometer using Cu Kα radiation and the scattering slits of 0.05^o. And the wide-angle XRD patterns of the supports and catalysts were measured on a powder X-ray diffractometer (Shimadzu XRD 6000) using Cu Kα (λ = 0.15406 nm) radiation and with a scanning rate of 4^o/min. The UV–Vis diffuse reflectance spectroscopy (UV–Vis DRS) experiments were performed on a UV–Vis spectrophotometer (Hitachi U-4100) with the integration sphere diffuse reflectance attachment. And the powder catalysts were loaded in a transparent quartz cell and characterized in the region of 200–800 nm at room temperature. The Raman spectra were obtained using a Renishaw Raman InVia Microscope (Spectra-Physics model 163), operated at the argon ion laser with wavelength of 244, 325 and 532 nm. The laser spot size was approximately 1–2 μm with a power of 3.6 mW. Fourier transform infrared (FT-IR) spectra were obtained by a FTS-3000 spectrophotometer (American Digilab Company). The nature of the acid sites over the catalysts was determined by pyridine-FTIR on a MAGNAIR 560 FTIR instrument (Nicolet Co., US) with a resolution of 1 cm^{-1}. The surface morphology and SEM-EDX elemental mapping of the supports and catalysts was observed by field emission scanning electron microscopy (SEM) on a Quanta 200F instruments using accelerating voltages of 20 kV. TEM images were taken from thin edges of particles supported on a porous carbon grid using a JEOL JEM 2100 electron microscope operated at 120 kV. The pore size distributions and surface areas of the samples were obtained by nitrogen isotherms using a Micromeritics ASAP 2010 system at liquid nitrogen temperature.

2.4 Catalytic activity

The full-range FCC gasoline used in this study was obtained from Sinopec Shijiazhuang Refining & Chemical Company. The hydro-upgrading performance of CoMo supported catalysts were evaluated in fixed-bed reactor with 2 g catalyst. Before the reactions, all of the catalysts were presulfided for 4 h with H_2 and 2 wt% CS_2 in cyclohexane under the temperature of 320 ^oC and the pressure of 2.5 MPa. The hydro-upgrading reactions were carried out under the condition of 270 ^oC, 2.0 MPa, H_2/hydrocarbon ratio of 200 mL/mL and weight hourly space velocity (WHSV) of 2.0 h^{-1}. After steady state was reached, the liquid product was collected, and the sulfur content was tested by a RPP-2000SN sulfur & nitrogen analyzer (Taizhou Central Analytical Instruments Co. Ltd. P.R. China). The RON values and lumped compositions of feedstock and products were analyzed in a Beifen 3420A gas chromatograph with a PONA capillary column (50 m×0.2 mm×0.5 μm) by the data-processing software GC99 (Beijing Research Institute of Petroleum Processing, SINOPEC, P.R. China).
The HDS conversion of FCC gasoline is expressed by:

$$\mathbf{HDS}(\%) = \frac{\mathbf{S_f - S_P}}{\mathbf{S_f}} \times \mathbf{100} \quad (1)$$

where the S_f and S_p represent the sulphur contents (mg/L) of the feedstock and products, respectively.
The RON loss during the reactions is calculated according to the following equation:

$$\mathbf{\Delta RON = RON_p - RON_f} \quad (2)$$

Where RON_p and RON_f are the RON values of products and feedstock, respectively.
The conversion of olefin is defined as follows:

$$\mathbf{OHY}(\%) = \frac{\mathbf{O_f - O_P}}{\mathbf{O_f}} \times \mathbf{100} \quad (3)$$

where the O_f and O_p are the mass fractions of olefins in the feedstock and products, respectively.
The selectivity factor (HF) is defined as the ratio of (HDS) activity to OHY activity and is expressed by[22]:

$$\mathbf{HF} = \frac{\mathbf{\ln(S_f/S_p)}}{\mathbf{\ln(O_f/O_p)}} \quad (4)$$

3 Results and discussion

3.1 Characterization of Beta-SBA-15 with different morphologies

The low angle and wide angle XRD patterns of Beta-SBA-15 composite materials synthesized from the Beta nanocrystals with different crystallization times are displayed in Fig. S1A and S1B, respectively. In Fig. S1A, the Beta-SBA-15 all exhibit three well-resolved diffraction peaks in the low angle

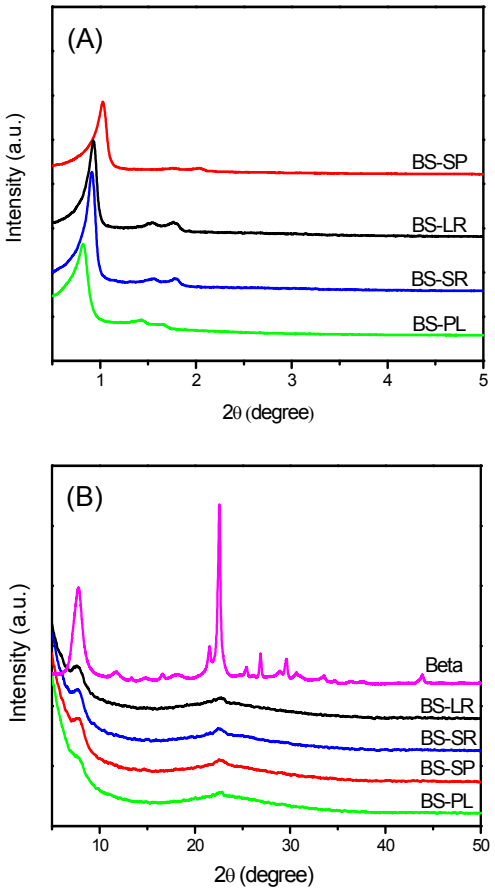

Fig. 1. XRD patterns of Beta-SBA-15 composites with different morphologies in the low angle (A) and wide angle domains (B).

domain, indexed as (100), (110) and (200) reflections respectively, which indicates that they all possess hexagonal (p6mm) symmetry and well-ordered mesoporous structure.[26, 27] Moreover, from the wide angle domain in Fig. S1B, the relative crystallinity of Beta zeolite increases with increasing the crystallization time. The larger Beta nanocrystals cannot be constructed into the framework of SBA-15. Therefore, the relative crystallinity of Beta-SBA-15 composite decreases with the increasing of crystallization time of Beta nanocrystals. In this research, the best crystallization time of Beta nanocrystals is 12 h.

The XRD patterns of Beta-SBA-15 with different morphologies are shown in Fig. 1. It can be seen from Fig. 1A that the platelet, sphere, short-rod and long-rod Beta-SBA-15 materials all have three well-resolved diffraction peaks, representing for (100), (110) and (200) reflections, respectively, demonstrating that these different materials possess a similar structure to P6mm hexagonal mesoporous material. The XRD patterns of Beta-SBA-15 with different morphologies in the wide angle domains are listed in Fig. 1B, which show that the Beta zeolite possesses very intense characteristic peaks at 7.6° and 22.4°.[28] And the Beta-SBA-15 materials also have the same diffraction peaks as zeolite Beta but with relatively low

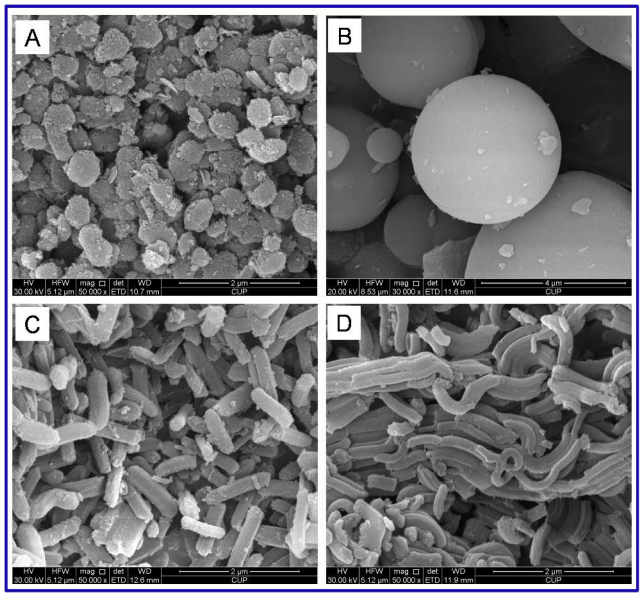

Fig. 2. SEM images of the as-synthesized Beta-SBA-15 with platelet (A), sphere (B), short-rod (C) and long-rod (D) morphologies.

intensity. Therefore, it can be demonstrated from the results of XRD that the as-synthesized Beta-SBA-15 materials possess both SBA-15 and Beta zeolite structures.

The morphology of Beta-SBA-15 was investigated by means of field emission SEM. Fig. 2A-D shows the changes of particle size and morphology of Beta-SBA-15 materials. The different synthesis temperature, cosurfactant and electrolyte in the synthesis procedure can result in different morphology of the composite. This phenomenon may be correlated to the local curvature energy that is present at the interface of amphiphilic block copolymer species and the inorganic silica. The platelet Beta-SBA-15 (Fig. 2A) was formed by introducing a small amount of Zr(IV) ions in the synthesis solution. The Zr(IV) ions may have two effects in the synthesis process. The first is the so-called salting-out effect, in which the highly solvated species reduce the critical micellar concentration value of P123 triblock copolymer. Secondly, it probably increase the local concentration of TEOS around P123 micelles.[20] The sphere Beta-SBA-15 material with average particle size in 4.6 μm can be constructed by using the cationic surfactant CTAB as a cosurfactant, which suggests that the addition of CTAB can lower the local curvature energy and conduce to the formation of sphere shape. Fig. 2C and 2D show the short-rod and long-rod Beta-SBA-15, respectively. The width and length of short-rod Beta-SBA-15 (Fig. 2C) are ~320 nm and ~1000 nm, respectively, while the long-rod Beta-SBA-15 (Fig. 2D) are ~200 nm and ~1400 nm, respectively, demonstrating that the synthesis temperature has an effect on the morphology of Beta-SBA-15. In addition, the SEM-EDX elemental mapping was also performed to detect the elemental content and distribution (Fig. S2-S5). The results from SEM-EDX elemental mapping analysis show that the Al species are uniform distributed in the Beta-SBA-15 materials with platelet, sphere, short-rod, and long-rod morphologies, indicating that the Beta zeolite seeds

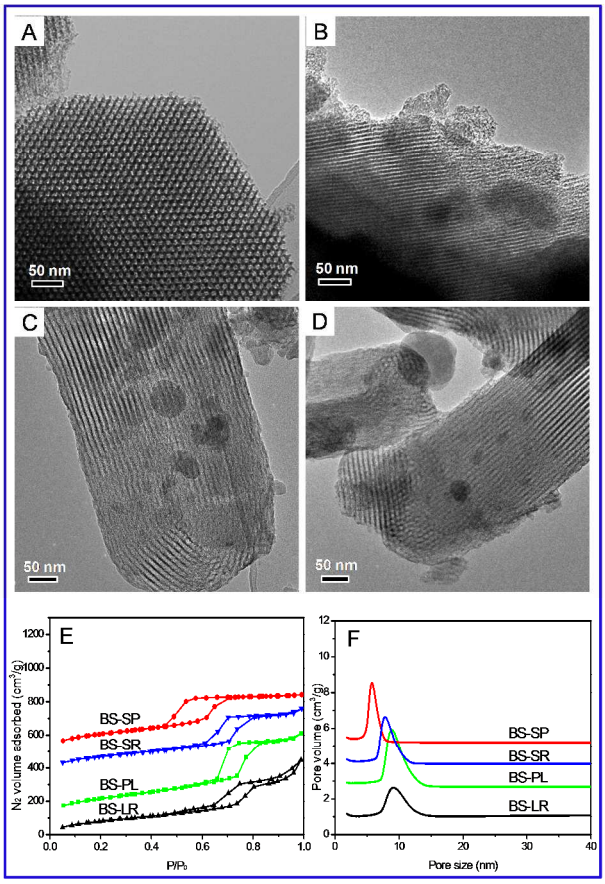

Fig. 3. TEM images of the as-synthesized Beta-SBA-15 materials with platelet (A), sphere (B), short-rod (C) and long-rod (D) morphologies; and the corresponding N_2 adsorption-desorption isotherms (E) and pore size distribution curves (F).

could be evenly distributed in the structure of SBA-15. The EDX spectra of these materials (Fig. S2-S5) reveal that the loading of Al species is more than the raw materials, demonstrating a part of Si species lost during the synthesis procedure. And the Al contents of sphere and platelet Beta-SBA-15 are slightly higher than that of short-rod and long-rod Beta-SBA-15, which indicates the Al species can be more easily embedded into sphere and platelet Beta-SBA-15 structures than the other two materials.

The TEM images of Beta-SBA-15 materials are displayed in Fig. 3. It is difficult to discern the microporous BEA topology structure of zeolite Beta, while BS-SR, BS-LR, BS-PL and BS-SP exhibit well ordered arrays of mesopores, demonstrating that they all have 2D *P6mm* hexagonal structures, which is consistent with the previous XRD results. TEM images in Fig. 3C and 3D verify that the mesochannels of Beta-SBA-15 with rod morphologies run along the length direction of the particles. And the mesochannels of sphere SBA-15 in Fig. 3B grow along with the diameter of the sphere. The large pores (5.5–8.5 nm) of Beta-SBA-15 are clearly visible in their TEM images. Moreover, some nano-sized Beta seeds were encapsulated in the structure of short-rod and long-rod Beta-SBA-15 materials.

The N_2 adsorption-desorption isotherms of Beta-SBA-15 with different morphologies and the corresponding pore size distribution curves are also shown in Fig. 3E and 3F, respectively. All the isotherm patterns of BS-PL, BS-SP, BS-SR and BS-LR show the type IV curves with a H1 hysteresis loop which is typical of mesoporous materials with 2D cylindrical channel.[29] The isotherm exhibits a sharp inflection in the P/P_0 range from 0.50 to 0.85 that is a characteristic of capillary condensation within uniform mesostructure. These results coincide with that of XRD and TEM. The pore size distributions of BS-PL, BS-SP, BS-SR and BS-LR, calculated from the adsorption branch of the isotherms, show a narrow distribution of mesopores. The textural and structural characteristics of the supports are summarized in Table 1. The pore diameters of the composites follow the order of BS-SP (5.7 nm) < BS-SR (7.6 nm) < BS-PL (8.0 nm) < BS-LR (8.2 nm) which can be also obtained from pore size distribution curves in Fig. 3F. The Beta-SBA-15 materials with different morphologies have different surface areas with the order of BS-SR (695 m^2/g) < BS-PL (698 m^2/g) < BS-LR (701 m^2/g) < BS-SP (750 m^2/g). These data indicate that the Zr(IV) ions and high synthesis temperature can increase the pore diameter of Beta-SBA-15 composite. And the cosurfactant CTAB can enhance the surface area of the composite. Moreover, the Zr(IV) ions and cosurfactant CTAB also improve the pore volume of the material.

Table 1. Textural and structural characteristics of the as-synthesized materials with different morphologies.

Samples	Morphology	S_{BET}[a] (m^2/g)	V_t[b] (cm^3/g)	V_{mes}[c] (cm^3/g)	V_{mic}[d] (cm^3/g)	d_{BJH}[e] (nm)
BS-PL	Platelet	698	0.92	0.81	0.07	8.0
BS-SP	Sphere	750	0.70	0.58	0.12	5.7
BS-SR	Short-rod	695	0.88	0.73	0.12	7.6
BS-LR	Long-rod	701	0.76	0.61	0.12	8.2
SBA-15	—	686	1.08	1.01	0.07	6.4
Beta	—	502	0.34	—	0.22	—

[a]Calculated by the BET method. [b]The total pore volume was obtained at a relative pressure of 0.98. [c]Calculated using the BJH method. [d]Calculated using the t-plot method. [e]Mesopore diameter calculated using the BJH method.

The FT-IR spectra of Beta-SBA-15 materials with different morphologies are shown in Fig. 4A. The framework vibration spectra of Beta-SBA-15 consist of the bands centered at 805, 955, and 1035 cm^{-1}, which are similar to the SiO_2-based mesoporous materials. These three bands are assigned to the Si–O–Si symmetric stretching vibrations, the defective Si–OH groups and the Si–O–Si asymmetric stretching vibrations, respectively.[30] Moreover, two additional bands (520 cm^{-1} and 570 cm^{-1}) attributed to zeolite Beta (the six or five rings of characteristic structure of BEA-type zeolites) are also detected[31].

The UV Raman spectra of the as-synthesized materials excited with the laser at 244 nm was performed to investigate the coordination environments of the framework and the results are presented in Fig. 4B. The Raman spectroscopy of zeolite Beta is difficult to be obtained because of its low symmetry and

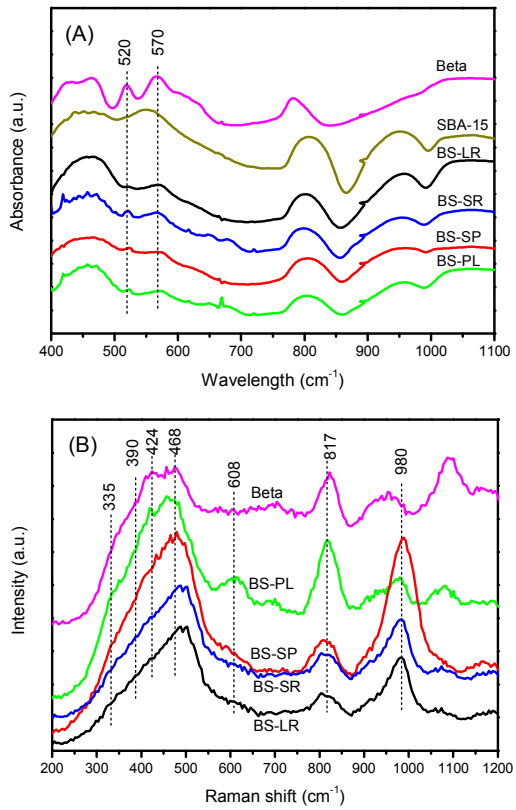

Fig. 4. FT-IR spectra (A) and Raman spectra excitation at 244 nm (B) of Beta-SBA-15 materials with different morphologies.

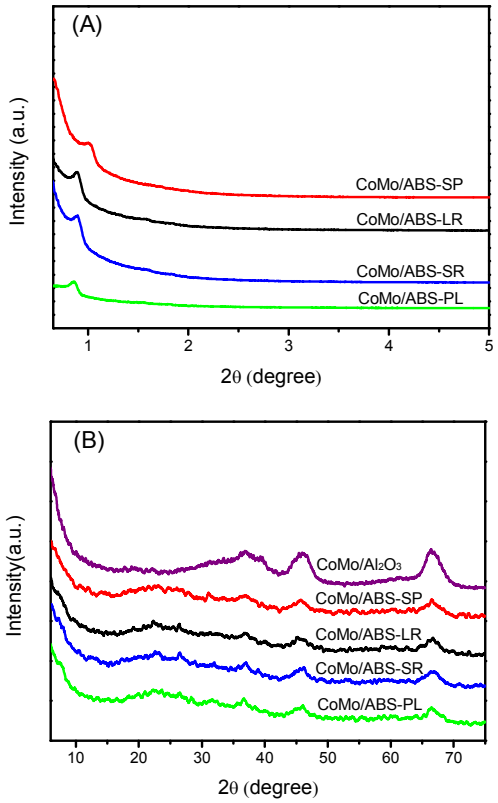

Fig. 5. XRD patterns of the CoMo catalysts in the low angle (A) and wide angle domains (B).

strong background fluorescence. As shown in Fig. 4B, the bands of Beta-SBA-15 ascribed to Beta zeolite are not obvious. The results show that the bands at 335, 390, 424, 468, 608, 817 and 980 cm^{-1} are detected over the as-synthesized materials. According to literature, the band at 335 cm^{-1} and 390 cm^{-1} are attributed to the bending mode of the six-membered rings and five-membered rings of BEA-type zeolites, respectively, and the bands at 424 and 468 cm^{-1} are ascribed to the bending mode of the four-membered rings.[32] The bands at 608 cm^{-1} is assigned to the three and four siloane rings of SBA-15, and the bands at 817 and 980 cm^{-1} are assigned to the symmetrical Si-O-Si stretching mode and the Si-OH stretch of surface hydroxyl groups, respectively.[33] These results are consistent with the FT-IR spectra.

3.2 Characterization of the supported CoMo catalysts

Fig. 5 shows the XRD patterns of CoMo oxide catalysts supported on different materials. It can be found in Fig. 5A that the characteristic peaks of the SBA-15 still present, indicating that the mesoporous structure is reserved after the supports mixed with γ-Al_2O_3 and loaded with the active metal components. The wide-angle XRD patterns of CoMo supported catalysts in Fig. 5B show that three characteristic peaks appear at 2θ=36.8°, 46.2° and 66.7° are attributed to γ-Al_2O_3. And the XRD patterns in Fig. 5B also demonstrate that MoO_3 is well dispersed on the support surfaces since almost no bulk MoO_3 is detected in the range from 12° to 35°.[34]

The UV-vis diffuse reflectance spectroscopy was applied to determine the nature of the coordination and aggregation state of Mo oxidic species in the catalysts in the wavelength range of 200–800 nm. And the UV–vis DRS spectra of the oxide CoMo catalysts with different morphologies are listed in Fig. 6. It can be seen from Fig. 6 that the absorption in the 200–400 nm region should be associated to the ligand-metal charge transfer band (LMCT) $O^{2-} \rightarrow Mo^{6+}$.[35] All the catalysts showed absorption signals at wavelength shorter than 350 nm, indicating no aggregated MoO_3 species.[36] The bands at 260–280 nm are commonly assigned to the tetrahedral molybdate, whereas the band in the higher region 280–330 nm is attributed to the polymolybdate (octahedral) species. Moreover, the broad band at 260–350 nm was detected on all the catalysts, indicating both the tetrahedral and octahedral molybdates can be present on all the corresponding catalysts. These octahedron Mo species are more inclined to form the coordinatively unsaturated or sulfur vacancies, which favor the hydrodesulfurization reaction. All the catalysts possess high proportion of octahedral Mo^{6+}. In addition, a broad band in the region 450–700 nm is observed in all the catalysts especially CoMo/γ-Al_2O_3. The triplet band centered at 575 nm is ascribed to tetrahedral cobalt (II) ions which are formed at temperature above 623 K.

The Raman spectrum is sensitive to the crystalline symmetry and reflects the nature of the oxide phases supported on the

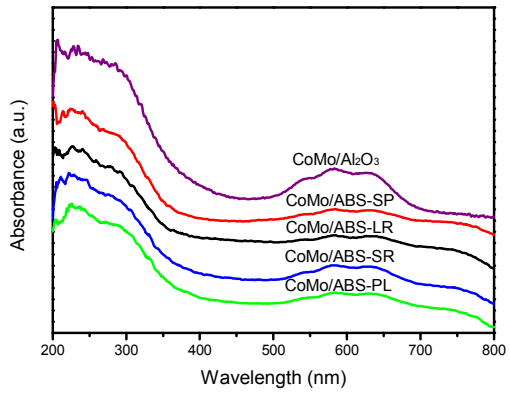

Fig. 6. UV–Vis DRS spectra of the oxide CoMo catalysts.

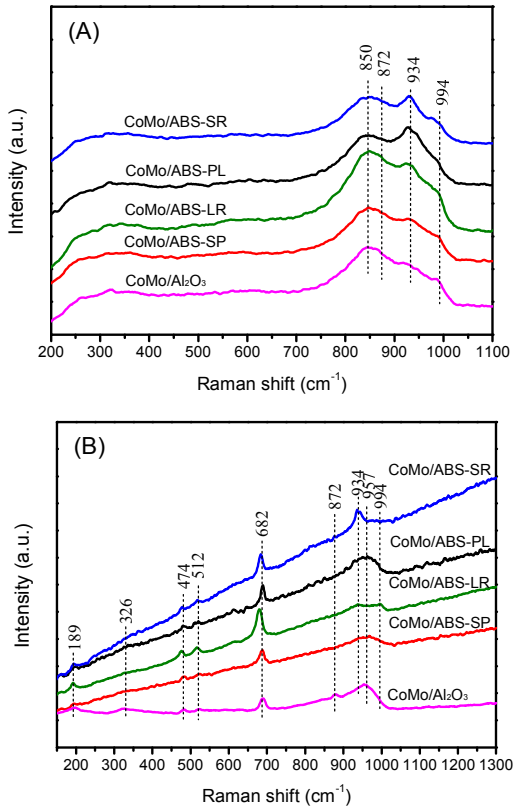

Fig. 7. Raman spectra of different catalysts excitation at 325 nm (A) and 532 nm (B).

catalyst. The Raman spectra of the CoMo catalysts excitation at 325 nm and 532 nm are displayed in Fig. 7. The Visible Raman spectra (532 nm) of CoMo catalysts display strong background fluorescence. Therefore, we used the UV Raman spectra (325 nm) for comparison. It can be found in Fig. 7A that the peaks at 934, 872 and 814 cm^{-1} existed in all the catalysts are ascribed to the Mo-O bond stretching of two crystallographically in equivalent tetrahedral coordinated Mo^{6+} presented in $CoMoO_4$ structure.[37] The band at 994 cm^{-1} is assigned to the crystalline MoO_3 supported on the catalysts.[38] And the peak intensity of crystalline MoO_3 over CoMo/ABS-SP and CoMo/ABS-PL is relatively weaker than other catalysts, indicating that the amorphous phase of MoO_3 are well dispersed on the mesochannels and surfaces of ABS-SP and ABS-PL. In comparison, the Visible Raman spectra of these catalysts in Fig. 7B reveal that there are more peaks assigned to the molybdenum and cobalt species in spite of the strong background fluorescence. The bands at 872 and 934 cm^{-1} are also detected on the catalysts using Visible Raman. In addition, the band at 957 cm^{-1} over the CoMo/ABS-SP, CoMo/ABS-PL and CoMo/γ-Al_2O_3 catalysts is associated with the symmetric stretching and bending modes of the terminal Mo=O bond.[39] The peaks at 682 and 474 cm^{-1} over these catalysts are assigned to Co_3O_4 spinel-type structure.[40] And the band at 512 cm^{-1} may be related to the $CoAl_2O_4$.[41]

The dispersion of MoS_2 crystallites over these catalysts can be obtained from the HRTEM images of the sulfided catalysts. The slab length and layer stacking distributions were obtained through the statistical analyses based on 300 slabs. The average slab length (*Lav*) and stacking layer number (*Nav*) were calculated according to the following equation:

$$\boldsymbol{L_{av}(N_{av})} = \frac{\sum_{i=1}^{n} x_i M_i}{\sum_{i=1}^{n} x_i} \quad \textbf{(5)}$$

where x_i is the number of slabs or stacks in the particles and M_i denotes as the stacking layer number or the length of the slab particles. The dispersion degree of Mo (f_{Mo}) is determined from the following equation[42, 43]:

$$\boldsymbol{f_{Mo}} = \frac{\sum_{i=1}^{t} (6n_i - 6)}{\sum_{i=1}^{t} (3n_i^2 - 3n_i + 1)} \quad \textbf{(6)}$$

where the numerator is the number of atoms located on the edges and the denominator is the total number of Mo atoms; t is the total number of slabs and n_i is the number of Mo atoms along one edge of a MoS_2 slab determined from the length (L=3.2(2n_i-1)Å) observed by HRTEM.

Table 2. Average length (*L*av) and average stacking number (*N*av) of MoS_2 crystallites.

catalyst	*Lav* (nm)	*Nav*	f_{Mo}
CoMo/ABS-PL	2.9	2.5	0.36
CoMo/ABS-SP	3.1	2.9	0.33
CoMo/ABS-SR	3.2	2.4	0.32
CoMo/ABS-LR	3.3	2.3	0.31
CoMo/γ-Al_2O_3	4.4	2.2	0.24

The HRTEM micrographs of the five sulfided catalysts are displayed in Fig. 8A-E. The length and stacking layer number distributions of MoS_2 slabs on sulfided catalysts are also shown in Fig. 8. The average length (*Lav*) and stacking number (*Nav*) of MoS_2 crystallites are listed in Table 2. The average length of MoS_2 slabs on the sulfided catalysts follows the order of CoMo/ABS-PL (2.9 nm) < CoMo/ABS-SP (3.1 nm) < CoMo/ABS-SR (3.2 nm) < CoMo/ABS-LR (3.3 nm) < CoMo/γ-Al_2O_3 (4.4 nm). The average stacking layer number of

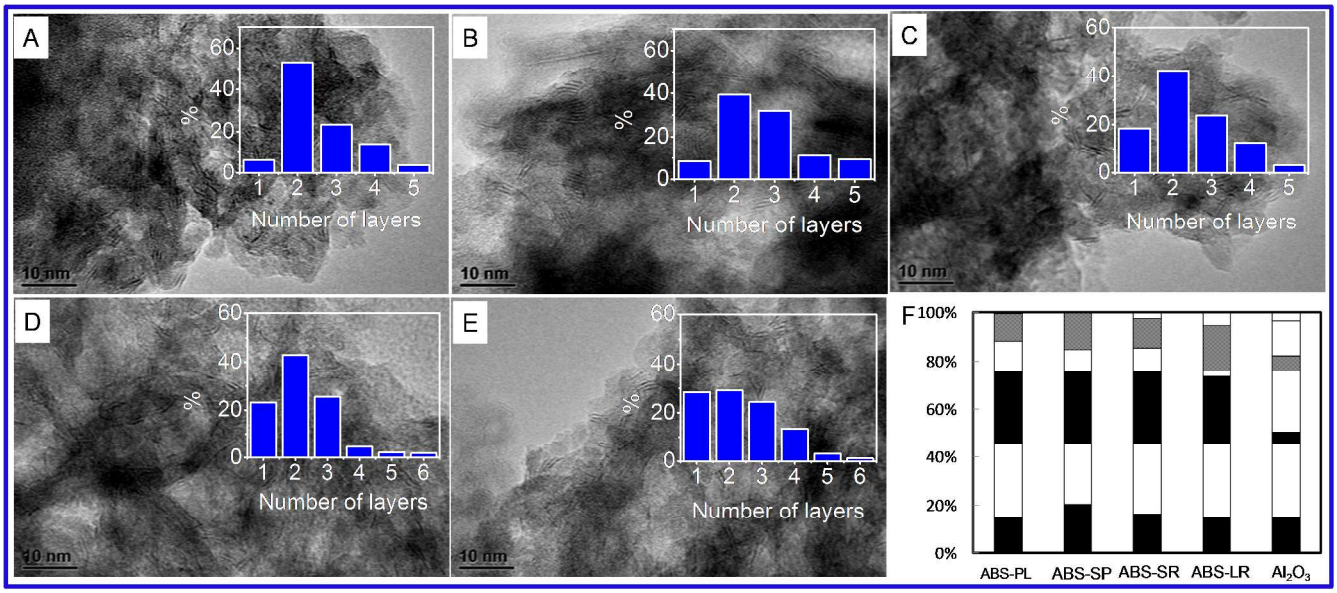

Fig. 8. HRTEM images of the sulfided catalysts: (A) CoMo/ABS-PL, (B) CoMo/ABS-SP, (C) CoMo/ABS-SR, (D) CoMo/ABS-LR, (E) CoMo/γ-Al_2O_3; (F) the distribution of length in Å of the MoS_2 particles dispersed on the supported catalysts, (■) 0–20, (■) 21–40, (■) 41–60, (■) 61–80, (□) 81–100.

MoS_2 slabs on these catalysts follows the order: CoMo/γ-Al_2O_3 (2.2) < CoMo/ABS-LR (2.3) < CoMo/ABS-SR (2.4) < CoMo/ABS-PL (2.5) < CoMo/ABS-SP (2.9). It can be observed that CoMo/γ-Al_2O_3 shows strong interactions between the MoS_2 phase and the alumina support, which possesses the longest length (4.4 nm) and the lowest stacking number (2.2) of MoS_2 slabs. The catalysts doped with Beta-SBA-15 materials exhibit short length and suitable stacking number of the MoS_2 slabs, which have high HDS performance. Among them, the CoMo/ABS-PL catalyst has the shortest length (2.9) and suitable stacking number (2.5) of the MoS_2 slabs which possesses the largest f_{Mo} value of 0.36. In summary, the f_{Mo} values of CoMo supported catalysts follow the order: CoMo/γ-Al_2O_3 (0.24) < CoMo/ABS-LR (0.31) < CoMo/ABS-SR (0.32) < CoMo/ABS-SP (0.33) < CoMo/ABS-PL (0.36).

As well known, the acidity of the catalysts has great influence on the hydrodesulfurization reactions. The Pyridine IR spectroscopy is an efficient technology to determine the strength and acid type of the catalysts.[44] And the FT-IR spectra of the catalysts after pyridine evacuation at 200 and 350 °C are listed in Fig. S7A and S7B, respectively. The bands located at 1453 cm^{-1} and 1576 cm^{-1} are attributed to pyridine adsorbed on Lewis acid sites, and the band at 1542 cm^{-1} is assigned to pyridine adsorbed on Brönsted acid sites, while the band at1492 cm^{-1} is ascribed to the combination of Brönsted and Lewis acid sites.[45, 46] Fig. S7A clearly shows that a weak band at 1542 cm^{-1} presents in the spectra of CoMo/ABS-LR, CoMo/ABS-SR, CoMo/ABS-SP and CoMo/ABS-PL, demonstrating the existence of a small amount of Brönsted acid sites in these catalysts. But there is no Brönsted acid site existed over CoMo/γ-Al_2O_3 since the absence of the absorption band at 1542 cm^{-1} in the spectrum of CoMo/γ-Al_2O_3.

The acid strength distribution and the acid amounts of the catalysts are listed in Table 3. After degassing at 200 °C, the total acidity (Brönsted and Lewis) of the catalysts follows the order of CoMo/γ-Al_2O_3 < CoMo/ABS-LR < CoMo/ABS-SR < CoMo/ABS-PL < CoMo/ABS-SP which is consistent with the result of NH_3-TPD (Fig. S8). The acid amounts of CoMo catalysts supported on Beta-SBA-15 materials are much higher than that of CoMo/γ-Al_2O_3. The amounts of medium and strong acid sites (after degassing at 350 °C) over the catalysts are in the following order: CoMo/γ-Al_2O_3 < CoMo/ABS-LR < CoMo/ABS-SR < CoMo/ABS-SP < CoMo/ABS-PL. The different acid sites of the catalysts may be due to the different initial synthesis temperature. The high initial synthesis temperature can promote dealumination of Beta seeds during the synthesis of BS-LR and BS-SR in hydrochloric acid solution. Therefore, the acid sites of CoMo/ABS-LR and CoMo/ABS-SR are relatively lower than CoMo/ABS-SP and CoMo/ABS-PL. In addition, the Zr(IV) species embed in CoMo/ABS-PL may also increase the acidity of the catalyst due to its electronic modified effect.

Table 3. Amounts of B and L acid sites of the catalysts determined by pyridine-FTIR.

Catalysts	Amount of acid sites (μmol/g)					
	200 °C			350 °C		
	L	B	L+B	L	B	L+B
CoMo/ABS-PL	122.3	13.2	135.5	73.1	-	73.1
CoMo/ABS-SP	125.6	10.5	136.1	71.2	-	71.2
CoMo/ABS-SR	121.5	9.1	130.6	66.9	-	66.9
CoMo/ABS-LR	118.9	7.6	126.5	64.7	-	64.7
CoMo/γ-Al_2O_3	88.9	-	88.9	29.22	-	29.2

3.3 Catalytic performances in the hydro-upgrading of FCC gasoline

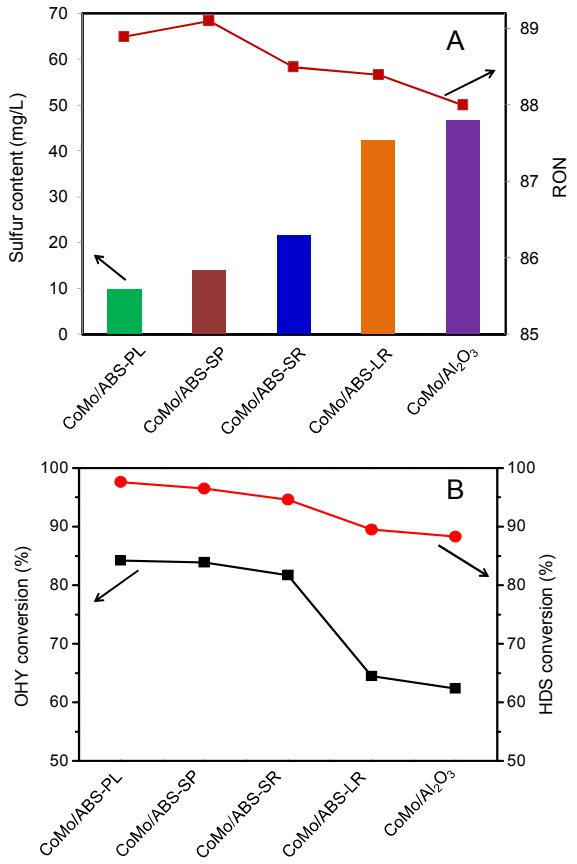

Fig. 9. The RON values and the sulfur contents of the products (A); the tendencies of the OHY and HDS activities over different catalysts (B).

The series of CoMo catalysts supported on Beta-SBA-15 with different morphologies were used to evaluate the hydro-upgrading performance of FCC gasoline, and the results are listed in Table 4. The CoMo/γ-Al_2O_3 catalyst exhibits a lower HDS efficiency (88.3 %) and a great loss of research octane number (2.2 unit) due to its excessive olefin saturation and low aromatization ability. CoMo/ABS-PL shows the highest HDS efficiency (97.6 %) and a relatively low RON loss (1.3 unit). The high HDS conversion of CoMo/ABS-PL may be assigned to its super hydrogenation ability. The CoMo/ABS-SP catalyst also possesses a high HDS efficiency (96.5 %) and the lowest RON loss (1.1 unit). The high i-paraffin (51.5 wt%) and aromatics (24.4 wt%) contents in the products are the main reasons for the high RON preservability of CoMo/ABS-SP. However, the CoMo/ABS-SR and CoMo/ABS-LR catalysts exhibit the relatively inferior catalytic performances which are related to their low hydrogenation, aromatization and isomerization abilities. In addition, the catalysts CoMo/ABS-PLM and Mo/ABS-PL with the low loading of CoO show the low HDS conversions and RON losses which may be also attributed to their poor hydrogenation abilities. The HDS conversions over these catalysts follow the order: Mo/ABS-PL (83.3 %) < CoMo/γ-Al_2O_3 (88.3 %) < CoMo/ABS-LR (89.5 %) < CoMo/ABS-PLM (91.3) < CoMo/ABS-SR (94.6 %) < CoMo/ABS-SP (96.5 %) < CoMo/ABS-PL (97.6 %), And the RON losses of the catalysts follow the order of Mo/ABS-PL (0.2 unit) < CoMo/ABS-PLM (0.8 unit) < CoMo/ABS-SP (1.1 unit) < CoMo/ABS-PL (1.3 unit) < CoMo/ABS-SR (1.6 unit) < CoMo/ABS-LR (1.8 unit) < CoMo/γ-Al_2O_3 (2.2 unit). The high activities of CoMo/ABS-SP and CoMo/ABS-PL are attributed to their superior physicochemical properties.

3.4 Effects of physicochemical properties of the catalysts on their catalytic performances

The hydro-upgrading performances of FCC gasoline over different catalysts are closely related to the physicochemical properties of the active metals and supports. The better properties of the supports are beneficial to the mass transfer, stability, and dispersion of the active metals. Among these influence factors, the mesochannel and acidity of the supports are the crucial parameters for FCC gasoline hydro-upgrading. A suitable amount of L and B acid sites and their synergistic effects are also important for FCC gasoline hydro-upgrading. The Brönsted acid sites can benefit C–S bond elimination and hydrogen transfer, while the Lewis acid sites on the catalysts may facilitate the adsorption and conversion of sulfides.[47] In this research, CoMo catalysts supported on Beta-SBA-15 materials with platelet, sphere, short-rod and long-rod morphologies were studied to clarify the relationship between the catalytic performances and their physicochemical properties.

It can be obtained from Fig. 9B that the trends of OHY and HDS conversions are almost synchronous during the process of hydro-upgrading over different catalysts, which are correlated to the hydrogenation ability of the catalysts. The hydrogenation ability is assigned to the dispersion and layer number of MoS_2. According to reference, Besenbacher et al.[48] proposed that the brim sites of MoS_2 slabs favour to break the S-C bond of thiophene to produce cis-2-butenethiolate and these sites are also able to hydrogenate thiophene to 2,5-dihydrothiophene. The brim active sites of MoS_2 slabs exhibit two functions of hydrogenolysis and hydrogenation. The CoMo/γ-Al_2O_3 catalyst has the lowest stacking number (2.2) of MoS_2 slabs which possesses the lowest brim active sites (f_{Mo}=0.24) and decreases the intrinsic hydrogenation ability. The platelet Beta-SBA-15 possesses the short mesochannels with large pore diameter and weak metal–support interactions, resulting in the highly stacked number (2.5) and short length MoS_2 (2.9 nm), which has more brim active sites (f_{Mo}=0.36) and increases the intrinsic activity. And the sphere Beta-SBA-15 with more mesopore cavities and large pore volume also have highly stacked (2.9) and short length MoS_2 (3.1 nm) with more brim active sites (f_{Mo}=0.33). However, the short-rod and long-rod Beta-SBA-15with mesochannel orifices existed only at the ends of the particles which have poor dispersion of the active components result in less brim active sites. Therefore, the hydrogenation abilities of the catalysts follow the order: CoMo/γ-Al_2O_3 < CoMo/ABS-LR < CoMo/ABS-SR < CoMo/ABS-SP < CoMo/ABS-PL.

Table 4. The hydro-upgrading results of FCC gasoline over different catalysts.

Cat.		Feed	CoMo/ ABS-PL	CoMo/ ABS-PLM	Mo/ ABS-PL	CoMo/ ABS-SP	CoMo/ ABS-SR	CoMo/ ABS-LR	CoMo/ γ-Al_2O_3
Lumped compositions of the liquid product (wt %)	n-Paraffin	6.0	10.7	9.7	8.1	10.1	11.0	9.8	13.0
	i-Paraffin	36.6	49. 5	43.6	42.0	51.5	50.9	48.4	47.3
	Olefin	27.9	4.4	14.9	18.7	4.5	5.0	9.9	10.5
	Naphthene	6.8	10.2	8.2	7.7	9.5	10.1	9.6	9.1
	Aromatics	22.7	25.2	23.6	23.5	24.4	23.0	22.3	20.1
RON		90.2	88.9	89.4	90.0	89.1	88.6	88.4	88.0
ΔRON			-1.3	-0.8	-0.2	-1.1	-1.6	-1.8	-2.2
S, mg/L		401.0	9.7	34.9	66.9	13.8	21.6	42.3	46.7
HDS%			97.6	91.3	83.3	96.5	94.6	89.5	88.3
OHY%			84.2	46.6	32.6	83.9	81.7	64.5	62.4
HF			2.0	3.9	4.6	1.9	1.7	2.2	2.2

Note: $\Delta RON = RON_p - RON_f$ (RON_p and RON_f are the RON values of the products and feedstock, respectively.); HDS is defined as the conversion of sulfur; OHY is the conversion of olefin; HF is defined as the ratio of HDS activity to OHY activity.

In addition, the morphologies and mesochannels of the supports also have an influence on the diffusion of the reactants and products during the reactions. The mesochannels with large and short unrestricted path length, such as platelet Beta-SBA-15 particles, are beneficial for eliminating the diffusion resistence. Moreover, the morphologies of the supports also play an important role in the dispersion of active components. The sphere Beta-SBA-15 micro-mesoporous material has more mesopore cavities over the external surface, and its internal surface has high connectivity. But the short-rod and long-rod Beta-SBA-15 have less mesochannel orifices. Therefore, the sphere Beta-SBA-15 material exhibits good diffusivity of reactants and the suitable dispersions of MoS_2 compared with the short-rod and long-rod Beta-SBA-15. The CoMo/ABS-PL and CoMo/ABS-SP catalysts with superior diffusion ability exhibit higher HDS conversions than other catalysts.

In addition to the dispersion of MoS_2, the Co promoter can also affect the C-S bond elimination and hydrogenation ability of the catalysts.[49] It can be found from the hydro-upgrading results in Table 4 and Fig. S10 that the CoMo/ABS-PL has much higher OHY and HDS abilities than Mo/ABS-PL, indicating that the Co promoter can improve the C-S bond elimination and hydrogenation ability of the catalysts. The excellent HDS ability of CoMo catalysts compared with that of the Mo supported catalysts may be explained by the weaker Co-S bond compared with the Mo-S bond, which will make a lower H_2S adsorption on the sulphur edge of the CoMo catalyst.[50] Therefore, the surface of CoMo catalysts will possess higher number of sulphur vacancies than that of the Mo catalysts. The hydrogenation abilities of the catalysts with different Co loading follow the order: Mo/ABS-PL < CoMo/ABS-PLM < CoMo/ABS-PL.

As listed in Table 3, γ-Al_2O_3-supported CoMo catalyst only contains abundant L acid sites which can facilitate the C-S bond scission and isomerization.[8] The Beta-SBA-15 materials possess B and L acid sites, simultaneously providing a positive effect on the aromatization, isomerization and HDS reactions, which contribute more to keep the RON value during the hydro-upgrading processes. In addition, the special pore structure of Beta zeolite can increase the aromatization and isomerization capability. The RON values in Fig. 9A display that the CoMo/ABS-SP and CoMo/ABS-PL possess high RON values while the RON values of CoMo/γ-Al_2O_3, CoMo/ABS-LR and CoMo/ABS-SR are relatively low due to their poor aromatization and isomerization abilities. The higher RON values of the hydro-upgrading products over CoMo/ABS-SP (89.1) and CoMo/ABS-PL (88.9) are attributed to their more B and L acid sites. During the synthesis of Beta-SBA-15 materials, the temperatures of BS-SR and BS-LR in the stirring process are higher than BS-SP and BS-PL which can remove the aluminum of Beta zeolite and decrease the acidity of the materials. The higher total amounts of B and L acid sites over CoMo/ABS-PL and CoMo/ABS-SP catalysts also exhibit synergy effect on the hydroisomerization and aromatization.

According to reference,[51] the Brönsted and Lewis acid sites play important roles in hydroisomerization and aromatization during the hydro-upgrading process. It can be found in Fig. 10 that the isomerization (ISO) selectivity and the aromatization (ARO) selectivity are related to the amount of Lewis acid sites and Brönsted acid sites, which is consistent with the previous report.[8] The CoMo/ABS-SP and CoMo/ABS-SR catalysts with more Lewis acid sites possess high hydroisomerization (ISO) ability, while the CoMo/γ-Al_2O_3 has poor ISO selectivity (29.2 %) due to its less Lewis acid sites (Fig. 10A). In addition, the trends in Fig. 10A also show that the catalysts have a maximal hydroisomerization (ISO) activity with the increasing of B acid sites, demonstrating that a good balance between the amount of Lewis and Brönsted acid sites is required to achieve excellent hydroisomerization activity. The same phenomenon is observed in Fig. 10B. The single γ-Al_2O_3-supported CoMo

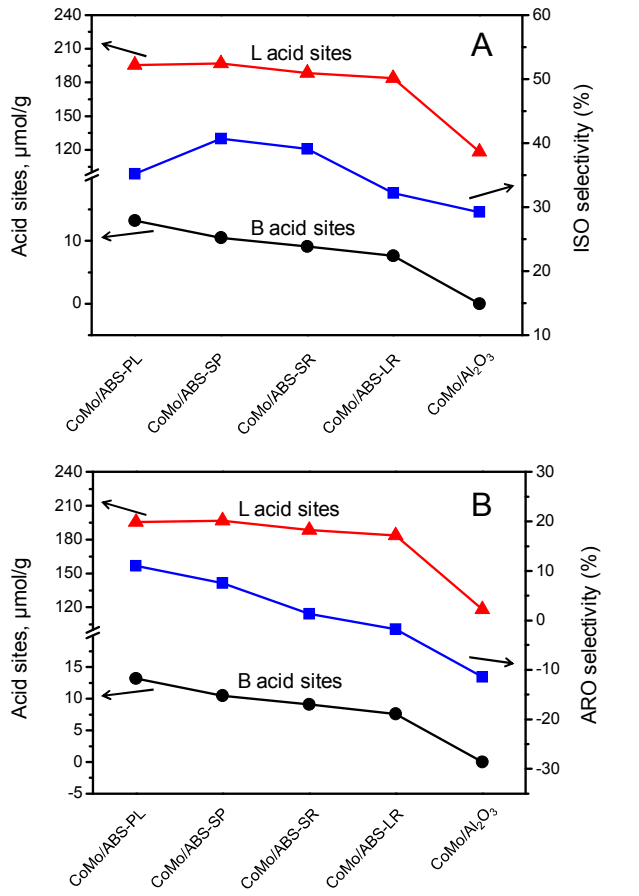

Fig. 10. The relationship of the acid amounts and the isomerization selectivity (A), and the aromatization selectivity (B) over different catalysts.

catalyst which only contains abundant L acid sites exhibits the lowest aromatization (ARO) selectivity (-11.4 %). With the introduction of B acid sites, the aromatization ability of the catalyst increases. The CoMo/ABS-PL which has the highest B acid sites endows with the best aromatization (ARO) selectivity (11.0 %). Therefore, the synergy between B and L acid sites would have a positive effect on the hydroisomerization and aromatization. In addition, the hydrogenation saturation and selective ring opening of aromatics occurred during the hydro-upgrading of FCC gasoline, so that the values of ARO selectivity over CoMo/ABS-LR and CoMo/γ-Al_2O_3 catalysts are negative due to their low ARO abilities.

4 Conclusions

In summary, a series of novel micro-mesoporous composites Beta-SBA-15 with platelet, sphere, short-rod, and long-rod morphologies were synthesized. The characterization results showed that the Beta-SBA-15 materials possess the similar mesoporous structure as SBA-15 and contain structural building units of microporous zeolite Beta. The synthesized Beta-SBA-15 materials exhibited different morphologies, pore sizes and surface areas, and the corresponding catalysts had different Lewis and Brönsted acid sites and dispersion degree of MoS_2. The platelet BS-PL possessed the short mesochannels with large pore diameter which enhanced the diffusion ability and increased the brim active sites of MoS_2. The sphere BS-SP had more mesopore cavities and suitable acidity, which can contribute to the hydroisomerization and aromatization. However, the short-rod BS-SR and long-rod BS-LR showed long mesochannels and less mesopore cavities, resulting in poor diffusion ability. The catalytic results demonstrated that the CoMo/ABS-PL exhibited the highest HDS conversion due to its superior hydrogenation and diffusion ability. The CoMo/ABS-SP catalyst with suitable B and L acid sites had the excellent RON preservation ability. Therefore, the diffusion of the supports and the synergy between B and L acid sites played an important role in HDS, hydroisomerization and aromatization activities. The platelet and sphere Beta-SBA-15 micro-mesoporous composites with outstanding physicochemical properties will be promising materials for FCC gasoline hydro-upgrading.

Acknowledgements

The authors acknowledge the financial supports from the NSFC (Nos. 21173269, 21276277 and U1463207), Ministry of Science and Technology of China (No. 2011BAK15B05), Specialized Research Fund for the Doctoral Program of Higher Education (20130007110003) and CNOOC Huizhou (HL00FW2012-0196).

Notes and references

[a] State Key Laboratory of Heavy Oil Processing, China University of Petroleum, Beijing 102249, PR China. E-mail: duanaijun@cup.edu.cn; zhangxin@cup.edu.cn

[b] Petrochemical Research Institute, PetroChina Company Limited, Beijing 100195, P. R. China.

[c] College of Science, China University of Petroleum, Beijing 102249, PR China.

1. C. Song, *Catal. Today*, 2003, **86**, 211-263.
2. I. V. Babich and J. A. Moulijn, *Fuel*, 2003, **82**, 607-631.
3. W. Han, P. Yuan, Y. Fan, G. Shi, H. Liu, D. Bai and X. Bao, *J. Mater. Chem.*, 2012, **22**, 25340.
4. Y. Fan, G. Shi and X. Bao, *AlChE J.*, 2013, **59**, 571-581.
5. T. Li, A. Duan, Z. Zhao, B. Liu, G. Jiang, J. Liu, Y. Wei and H. Pan, *Fuel*, 2014, **117**, 974-980.
6. Q. Huo, T. Dou, Z. Zhao and H. Pan, *Appl. Catal. A*, 2010, **381**, 101-108.
7. H. Topsøe, *Appl. Catal. A*, 2007, **322**, 3-8.
8. Y. Fan, D. Lei, G. Shi and X. Bao, *Catal. Today*, 2006, **114**, 388-396.
9. Q. Huo, Y. Gong, T. Dou, Z. Zhao, H. Pan and F. Deng, *Energy & Fuels*, 2010, **24**, 3764-3771.
10. A. Duan, G. Wan, Y. Zhang, Z. Zhao, G. Jiang and J. Liu, *Catal. Today*, 2011, **175**, 485-493.
11. X. Zhou, A. Duan, Z. Zhao, Y. Gong, H. Wu, J. Li, Y. Wei, G. Jiang, J. Liu and Y. Zhang, *J. Mater. Chem. A*, 2014, **2**, 6823-6833.
12. M. Á. Calderón-Magdaleno, J. A. Mendoza-Nieto and T. E. Klimova, *Catal. Today*, 2014, **220-222**, 78-88.
13. P. F. Fulvio, S. Pikus and M. Jaroniec, *J. Mater. Chem.*, 2005, **15**, 5049-5053.

14. Y. Li and B. Yan, *J. Mater. Chem.*, 2011, **21**, 8129-8136.
15. K. Waldron, Z. Wu, W. D. Wu, W. Liu, D. Zhao, X. D. Chen and C. Selomulya, *J. Mater. Chem. A*, 2014, **2**, 19500-19508.
16. D. Zhang, A. Duan, Z. Zhao and C. Xu, *J. Catal.*, 2010, **274**, 273-286.
17. Y. Li, D. Pan, C. Yu, Y. Fan and X. Bao, *J. Catal.*, 2012, **286**, 124-136.
18. S. Badoga, K. C. Mouli, K. K. Soni, A. K. Dalai and J. Adjaye, *Appl. Catal. B*, 2012, **125**, 67-84.
19. I. Agirrezabal-Telleria, J. Requies, M. B. Güemez and P. L. Arias, *Appl. Catal. B*, 2012, **115–116**, 169-178.
20. S.-Y. Chen, C.-Y. Tang, W.-T. Chuang, J.-J. Lee, Y.-L. Tsai, J. C. C. Chan, C.-Y. Lin, Y.-C. Liu and S. Cheng, *Chem. Mater.*, 2008, **20**, 3906-3916.
21. A. Katiyar, S. Yadav, P. G. Smirniotis and N. G. Pinto, *J. Chromatogr. A*, 2006, **1122**, 13-20.
22. Y. Fan, G. Shi, H. Liu and X. Bao, *Appl. Catal. B*, 2009, **91**, 73-82.
23. Y. Kang and C. B. Murray, *J. Am. Chem. Soc.*, 2010, **132**, 7568-7569.
24. J. Yu, Y. Yu, P. Zhou, W. Xiao and B. Cheng, *Appl. Catal. B*, 2014, **156–157**, 184-191.
25. H. I. Lee, J. H. Kim, G. D. Stucky, Y. Shi, C. Pak and J. M. Kim, *J. Mater. Chem.*, 2010, **20**, 8483.
26. D. Zhao, J. Feng, Q. Huo, N. Melosh, G. H. Fredrickson, B. F. Chmelka and G. D. Stucky, *Science*, 1998, **279**, 548-552.
27. D. Zhao, Q. Huo, J. Feng, B. F. Chmelka and G. D. Stucky, *J. Am. Chem. Soc.*, 1998, **120**, 6024-6036.
28. Q. Zhang, W. Ming, J. Ma, J. Zhang, P. Wang and R. Li, *J. Mater. Chem. A*, 2014, **2**, 8712-8718.
29. J. A. Melero, G. D. Stucky, R. van Grieken and G. Morales, *J. Mater. Chem.*, 2002, **12**, 1664-1670.
30. V. Umamaheswari, M. Palanichamy and V. Murugesan, *J. Catal.*, 2002, **210**, 367-374.
31. J. Perez-Pariente, J. A. Martens and P. A. Jacobs, *Applied Catalysis*, 1987, **31**, 35-64.
32. Y. Yu, G. Xiong, C. Li and F.-S. Xiao, *Microporous Mesoporous Mater.*, 2001, **46**, 23-34.
33. Y. Borodko, J. W. Ager, G. E. Marti, H. Song, K. Niesz and G. A. Somorjai, *J. Phys. Chem. B*, 2005, **109**, 17386-17390.
34. K. Soni, B. S. Rana, A. K. Sinha, A. Bhaumik, M. Nandi, M. Kumar and G. M. Dhar, *Appl. Catal. B*, 2009, **90**, 55-63.
35. T. Klimova, L. Peña, L. Lizama, C. Salcedo and O. Y. Gutiérrez, *Ind. Eng. Chem. Res.*, 2008, **48**, 1126-1133.
36. M. Cheng, F. Kumata, T. Saito, T. Komatsu and T. Yashima, *Appl. Catal. A*, 1999, **183**, 199-208.
37. T. Ono, N. Ogata and Y. Miyaryo, *J. Catal.*, 1996, **161**, 78-86.
38. J. Medema, C. van Stam, V. H. J. de Beer, A. J. A. Konings and D. C. Koningsberger, *J. Catal.*, 1978, **53**, 386-400.
39. B. Wang, G. Ding, Y. Shang, J. Lv, H. Wang, E. Wang, Z. Li, X. Ma, S. Qin and Q. Sun, *Appl. Catal. A*, 2012, **431–432**, 144-150.
40. C. F. Windisch, G. J. Exarhos and R. R. Owings, *J. Appl. Phys.*, 2004, **95**, 5435-5442.
41. B. Wang, Y. Yao, M. Jiang, Z. Li, X. Ma, S. Qin and Q. Sun, *Journal of Energy Chemistry*, 2014, **23**, 35-42.
42. S. Kasztelan, H. Toulhoat, J. Grimblot and J. P. Bonnelle, *Applied Catalysis*, 1984, **13**, 127-159.
43. O. Y. Gutiérrez and T. Klimova, *J. Catal.*, 2011, **281**, 50-62.
44. F. Zaera, *Chem. Soc. Rev.*, 2014, **43**, 7624-7663.
45. J. A. Z. Pieterse, S. Veefkind-Reyes, K. Seshan, L. Domokos and J. A. Lercher, *J. Catal.*, 1999, **187**, 518-520.
46. T. Kataoka and J. A. Dumesic, *J. Catal.*, 1988, **112**, 66-79.
47. G. B. McVicker, J. L. Kao, J. J. Ziemiak, W. E. Gates, J. L. Robbins, M. M. J. Treacy, S. B. Rice, T. H. Vanderspurt, V. R. Cross and A. K. Ghosh, *J. Catal.*, 1993, **139**, 48-61.
48. F. Besenbacher, M. Brorson, B. S. Clausen, S. Helveg, B. Hinnemann, J. Kibsgaard, J. V. Lauritsen, P. G. Moses, J. K. Nørskov and H. Topsøe, *Catal. Today*, 2008, **130**, 86-96.
49. M. Egorova and R. Prins, *J. Catal.*, 2006, **241**, 162-172.
50. M. Egorova and R. Prins, *J. Catal.*, 2004, **225**, 417-427.
51. Y. Fan, X. Lin, G. Shi, H. Liu and X. Bao, *Microporous Mesoporous Mater.*, 2007, **98**, 174-181.

Table of Contents Entry

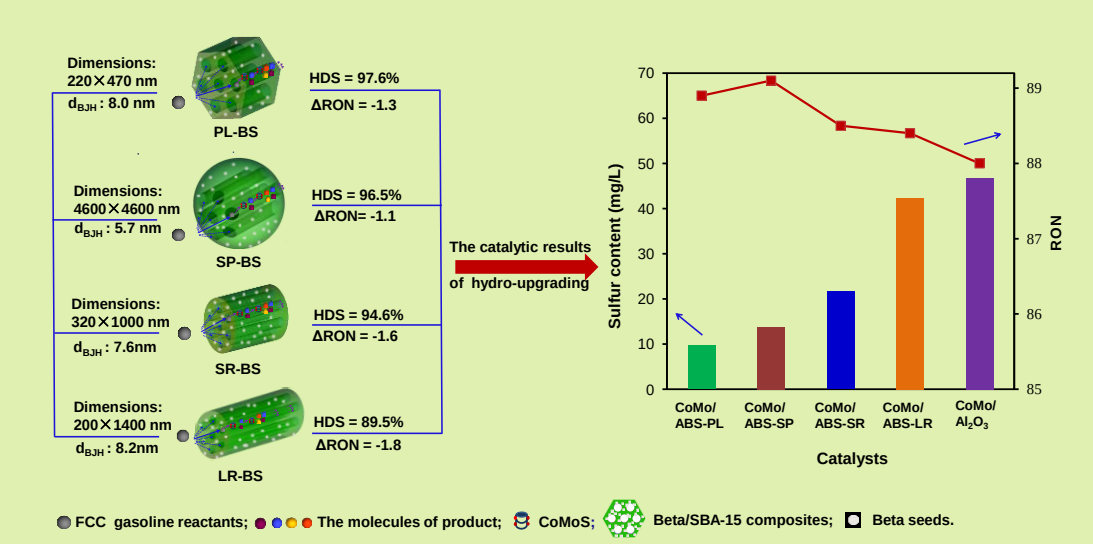

Micro-mesoporous Beta-SBA-15 materials with platelet, sphere, short-rod and long-rod morphologies were in-situ synthesized and used as the catalyst supports for hydro-upgrading of FCC gasoline. The outstanding physicochemical properties endow the platelet and sphere Beta-SBA-15 micro-mesoporous composites with excellent performances for FCC gasoline hydro-upgrading.